

Unusual Hole-doping-dependent Electronic Instability and Electron-Phonon Coupling in Infinite-layer Nickelates

Xuelei Sui^{1#}, Jianfeng Wang^{2,1#}, Xiang Ding³, Ke-Jin Zhou⁴, Liang Qiao³, Haiqing Lin^{1,5}, and Bing Huang^{1,5*}

¹*Beijing Computational Science Research Center, Beijing 100193, China*

²*School of Physics, Beihang University, Beijing 100191, China*

³*School of Physics, University of Electronic Science and Technology of China, Chengdu 610054, China*

⁴*Diamond Light Source, Harwell Campus, Didcot OX11 0DE, United Kingdom*

⁵*Department of Physics, Beijing Normal University, Beijing 100875, China*

[#]These authors contributed equally to this work.

*Correspondence should be addressed to B.H. (bing.huang@csrc.ac.cn).

The interplay between superconductivity and charge density waves (CDWs) under hole doping in cuprates is one of the central phenomena in condensed matter physics. Recently, CDWs are also observed in CaCuO₂-analogous nickelates $R\text{NiO}_2$ ($R = \text{La}, \text{Nd}$) but exhibit fundamentally different hole-doping-dependent behaviors compared to that in cuprates, raising a challenging question on its origin. In this article, we propose that electronic instability (EI) and moment-dependent electron-phonon coupling (MEPC), mainly contributed by Ni $3d_{x^2-y^2}$ and $R 5d_{z^2}$, respectively, may be the possible reasons for CDW formation in $R\text{NiO}_2$. Without hole doping, a strong Fermi surface nesting (FSN) induced by the unique feature of van Hove singularity (VHS) across Fermi level exists in $R\text{NiO}_2$ but not in CaCuO₂, and the unusual temperature-insensitive feature of EI and MEPC could result in rather high temperature CDWs in $R\text{NiO}_2$. Under hole doping, the reduced FSN of Ni $3d_{x^2-y^2}$ by the shift of VHS and decreased occupation of $R 5d_{z^2}$ largely weaken EI and MEPC in $R\text{NiO}_2$, respectively, suppressing the CDW formation. Our theory not only offers possible explanations to some puzzling experimental observations, but also establishes a unified understanding on the hole-doping-dependent EI and MEPC in nickelates and cuprates.

Introduction. Despite over 30 years of intense effort, the understandings of the physical origin accounting for the existence of high-temperature superconductivity [1-3] and competing symmetry-breaking orders [4,5] in cuprates remain the top challenges in condensed matter physics. A possible route to solve the puzzles in cuprates is to find other non-Cu-based superconductors but with cuprate-analogous structures [6,7]. Recently, the long-awaited superconductivity is eventually realized in hole-doped infinite-layer nickelates, *e.g.*, CaCuO₂-like RNiO₂ ($R = \text{La, Nd}$) [8,9], potentially bringing us to the new age of nickelates.

Besides of the superconductivity, charge density waves (CDWs), which are popular but competing or intertwining with superconductivity in cuprates [4,5,10], are also observed in LaNiO₂ [11] and NdNiO₂ [12,13]. In cuprates, the CDWs are usually absent in undoped systems but appear under certain hole doping concentrations (n_h) with a dome [5,14]. However, in nickelates, the CDWs appear in undoped LaNiO₂ [11] and NdNiO₂ [12,13] but becomes to monotonously weaken and eventually disappear without a dome, as Sr-doping-induced n_h increases, accompanied by the shift of q_{CDW} vector [11]. The possible mechanism for forming CDWs in RNiO₂, which is even under debate in cuprates [15-17], is largely unclear at this stage, as they might have multiple origins [18,19]. Since there is no clear evidence that hole doping can significantly change the electron correlation in RNiO₂ [20,21], we pay our attention to electronic instability (EI) and moment-dependent electron-phonon coupling (MEPC) in RNiO₂, as they are two of the major driving forces to form CDWs in solids [22,23]. In particular, we focus on a unified understanding of n_h -dependent behaviors of EI and MEPC in nickelates and cuprates, which may shed light on their significantly different n_h -dependent CDW evolutions.

In this article, using extensive first-principles calculations (see Methods), we propose that the intrinsic EI and MEPC may be possible reasons for the CDW formation in RNiO₂. Remarkably, different from the low-energy single-orbital physics in CaCuO₂, the Ni $3d_{x^2-y^2}$ and $R 5d_{z^2}$ play a larger role in contributing to EI and MEPC, respectively. In particular, the van Hove singularity (VHS) near the Fermi level (E_F) can induce strong Fermi surface nesting (FSN) at a series of k_z planes in undoped RNiO₂. As the n_h increases, the reduced FSN of Ni $3d_{x^2-y^2}$ due to the shift of VHS and the decreased occupation of $R 5d_{z^2}$ can gradually weaken the EI and MEPC in RNiO₂, respectively, eventually suppressing the CDW formation. These n_h -dependent behaviors of EI and MEPC in RNiO₂ are significantly different from those in CaCuO₂, due to the unique features of VHS and multiorbitals around E_F in RNiO₂. Surprisingly, both EI and MEPC are insensitive to the temperature, which may result in a rather high temperature CDW phase in undoped RNiO₂ (at least) up to 400 K, as confirmed by our preliminary experimental measurements (see Methods).

Multiorbital feature in RNiO₂. Figure 1(a) shows the schematic band structure of RNiO₂ and its analog CaCuO₂ in their nonmagnetic (NM) phase, extracted from the DFT calculations (Fig. S1 in Supplementary Information). In both RNiO₂ and CaCuO₂, the symmetry-allowed orbital coupling between in-plane $R/\text{Cu } 3d_{x^2-y^2}$ (majority) and $O 2p_x+p_y$ (minority) orbitals results in a delocalized band across the E_F . The bandwidth of $3d_{x^2-y^2}$ in RNiO₂ is ~ 1 eV narrower than that in CaCuO₂ [24,25]. One of the significant differences between RNiO₂ and CaCuO₂ is the presence of partially occupied low-lying $R 5d_{z^2}$ state across E_F in $k_z=0$ plane, which slightly hybridizes with Ni $3d_{z^2}$ orbital, leading to a multiorbital feature in RNiO₂ [26-29]. In contrast, Ca $3d_{z^2}$ is fully empty and

located at ~ 2 eV above E_F , resulting in a single-orbital feature in CaCuO_2 . Interestingly, the Lieb-type lattice formed by NiO_2 or CuO_2 plane creates VHSs at the boundary (X and R points) of Brillouin zone (BZ), as labeled by black arrows in Fig. 1(a). Importantly, in $R\text{NiO}_2$, the VHS is below E_F in $k_z=0$ plane but slightly above E_F in $k_z=0.5c^*$ plane, indicating that its E_F will exactly cross VHS in a specific k_z plane. However, differing from $R\text{NiO}_2$, all the VHSs in CaCuO_2 are located below E_F , partially due to the absence of Ca $5d_{z^2}$ state around E_F induced over occupation of $3d_{x^2-y^2}$ in CaCuO_2 . As illustrated below, the different locations of VHS between $R\text{NiO}_2$ and CaCuO_2 will lead to a delicate difference in their FS of $3d_{x^2-y^2}$ band and corresponding EI.

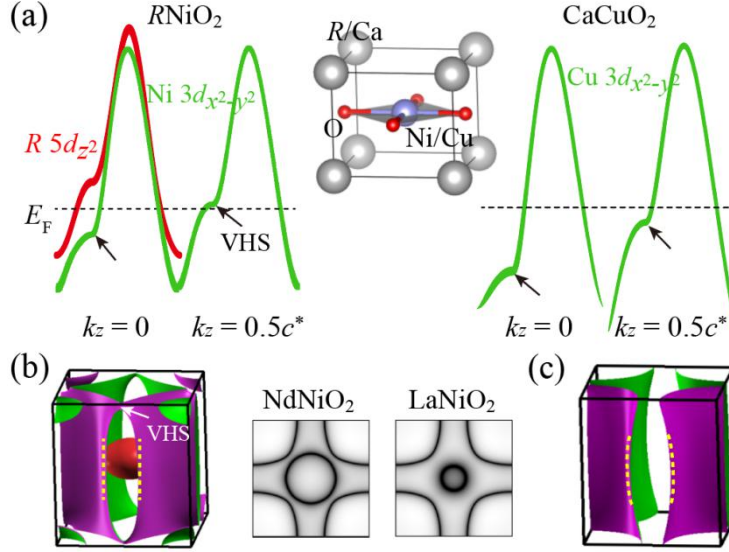


FIG. 1. (a) Comparison of low-energy electronic structures between $R\text{NiO}_2$ ($R=\text{Nd, La}$) and CaCuO_2 around E_F , in which only the dominated d orbital characters are presented. Inset: structure of $R\text{NiO}_2/\text{CaCuO}_2$. (b) Left: 3D FS of NdNiO_2 . Right: Cross sections of FSs in $k_z=0$ plane for NdNiO_2 and LaNiO_2 . VHSs are labeled by arrows in (a) and (b). (c) 3D FS of CaCuO_2 . Yellow-dashed lines in (b) and (c) highlight the FS evolutions along k_z .

The calculated FSs of undoped NdNiO_2 and CaCuO_2 are shown in Figs. 1(b) and 1(c), respectively. In both systems, the $3d_{x^2-y^2}$ orbital shows a cylinder-like hole pocket, exhibiting a quasi-2D-like dispersion. However, the existence of VHS at FS in NdNiO_2 but not in CaCuO_2 results in a noticeably different $3d_{x^2-y^2}$ FS between NdNiO_2 and CaCuO_2 . When k_z changes from $0.5c^*$ to 0, near VHS [labeled by the arrow in Fig. 1(b)], there is a significant momentum variation of FS in k_x-k_y plane; after passing through VHS, the energy band has a very large dispersion, and the shape of FS is almost unchanged in k_x-k_y plane with small k_z , exhibiting a nearly parallel segment of FS [highlighted by parallel lines in Fig. 1(b)]. This unusual FS feature, which is absent in (undoped) CaCuO_2 [highlighted by curved lines in Fig. 1(c)], is critical for the formation of strong FSN in $R\text{NiO}_2$ (also see Supplementary Fig. S1 for FS in $k_y = 0.5b^*$ plane). Another striking difference between NdNiO_2 and CaCuO_2 is the appearance of $5d_{z^2}$ state in the vicinity of Γ point [Fig. 1(a)], which forms a sphere-like electron pocket in NdNiO_2 [Fig. 1(b)], exhibiting an isotropic 3D dispersion. As for NdNiO_2 and LaNiO_2 , since the orbital energy of La $5d$ is higher than that of Nd $5d$, fewer $5d_{z^2}$ orbital is occupied in LaNiO_2 than in NdNiO_2 , resulting in a smaller electron pocket in LaNiO_2 [Fig. 1(b)]. As discussed later, this difference will result in weaker EI and MEPC in

LaNiO₂ than in NdNiO₂. We emphasize that all these unique features of FS remain unchanged even under the hybrid functionals or dynamical mean-field theory calculations [30,31].

Hole-doping-dependent EI and MEPC in RNiO₂. While the ground state of CaCuO₂ is an antiferromagnetic (AFM) Mott insulator [27], only local AFM fluctuations are observed in RNiO₂ [32,33], which even cannot coexist with the CDW phases in NdNiO₂ [12,13], possibly due to the competing between these different symmetry-breaking orders [3,4]. Meanwhile, although moderate hole doping can introduce superconductivity in both CaCuO₂ and RNiO₂, it could stabilize the CDW phases in CaCuO₂ [4] but weakens or even destroys the CDW phases in RNiO₂ [11,12]. Therefore, it is expected that the different low-energy orbital feature and FS (Fig. 1) could be responsible for different interplay between hole doping and CDW in RNiO₂ and CaCuO₂.

The real ($\text{Re}\chi$) and imaginary ($\text{Im}\chi$) parts of electron susceptibility (see Methods) reflect the EI and FSN of a system, respectively. Meanwhile, MEPC can be evaluated by calculating phonon linewidth γ (see Methods). Generally, the $\text{Re}\chi(\mathbf{q})$ and/or $\gamma(\mathbf{q})$ diverging at a wave vector \mathbf{q} might trigger a \mathbf{q} -modulated CDW [23]. In the following, we focus on the discussion of NdNiO₂ and briefly mention the results of LaNiO₂ in the main text.

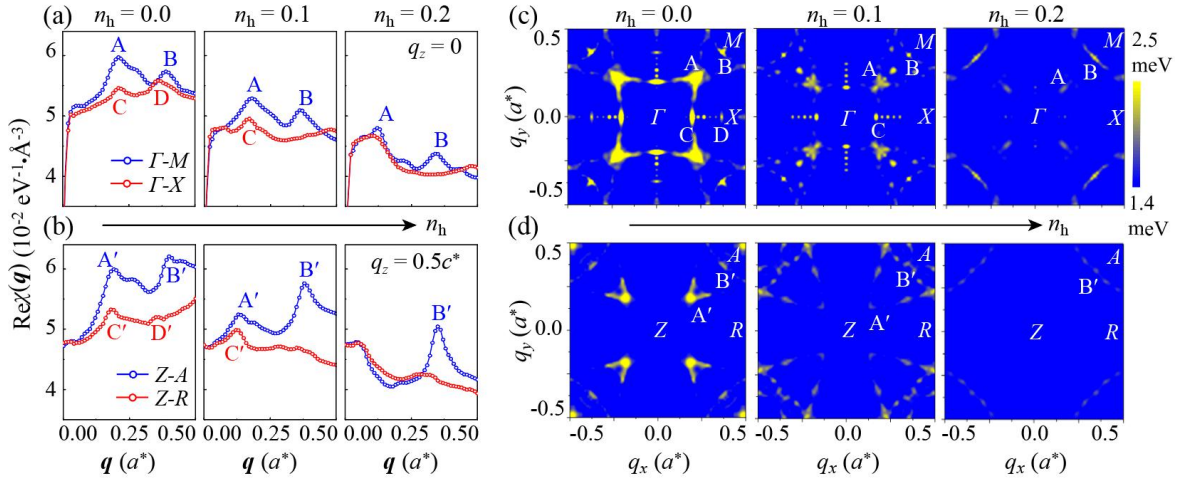


FIG. 2. (a) Calculated $\text{Re}\chi(\mathbf{q})$ of NdNiO₂ under three different n_h (in units of hole/u.c.) along two high-symmetry lines in $q_z = 0$ plane. (b) Same as (a) but in $q_z = 0.5c^*$ plane. (c) Calculated \mathbf{q} -resolved $\gamma(\mathbf{q})$ in $q_z = 0$ plane from all phonon modes for electronic states in entire BZ. (d) same as (c) but in $q_z = 0.5c^*$ plane. A (A'), B (B'), C (C'), and D (D') indicate the corresponding peak positions in $\text{Re}\chi(\mathbf{q})$ and $\gamma(\mathbf{q})$ at different \mathbf{q} .

Figures 2(a) and 2(b) show the calculated \mathbf{q} -dependent $\text{Re}\chi(\mathbf{q})$ in NdNiO₂ along two high-symmetry lines in $q_z = 0$ and $q_z = 0.5c^*$ planes, respectively. Especially, the calculated $\text{Re}\chi(\mathbf{q})$ in the entire BZ (Supplementary Fig. S2) confirm that the maxima of $\text{Re}\chi(\mathbf{q})$ are located in these lines. Overall, when $n_h = 0$, there are some similarities in these two planes, *i.e.*, there are multiple high-intensity peaks along Γ -M (Γ -X) and Z-A (Z -R) appearing at similar \mathbf{q} , reflecting a quasi-2D character of band structures. Importantly, these corresponding peaks in $\text{Re}\chi(\mathbf{q})$ are also observed in $\text{Im}\chi(\mathbf{q})$ (Supplementary Fig. S3), indicating that FSN plays important roles in forming the peaks in $\text{Re}\chi(\mathbf{q})$. Surprisingly, as the increase of n_h , the peak intensities of A, B (B') gradually decrease,

while the peaks of A', C (C'), and D (D') will eventually disappear; meanwhile, the corresponding \mathbf{q} for these peaks will gradually shift to smaller values. These unusual n_h -dependent behaviors are also observed in LaNiO_2 (Supplementary Fig. S4). To partially treat the electron-electron correlation effects, the on-site Hubbard U effects are also considered, which can further strengthen our conclusions (Supplementary Figs. S5-S7). Oposing to RNiO_2 , the peaks in $\text{Re}\chi(\mathbf{q})$ are very weak (almost absent) in undoped CaCuO_2 but become noticeable under certain n_h , along with the increased values of $\text{Re}\chi(\mathbf{q})$ (Supplementary Fig. S8).

Figures 2(c) and 2(d) show the calculated \mathbf{q} -dependent $\gamma(\mathbf{q})$ in $q_z = 0$ and $q_z = 0.5c^*$, respectively. Overall, when $n_h = 0$, the \mathbf{q} for generating high-intensity peaks in $\gamma(\mathbf{q})$ are consistent with that in $\text{Re}\chi(\mathbf{q})$, although the relative intensities for different peaks are slightly different in $\text{Re}\chi(\mathbf{q})$ and $\gamma(\mathbf{q})$. Interestingly, the C' and D' peaks can only exist in $\text{Re}\chi(\mathbf{q})$ but not in $\gamma(\mathbf{q})$. Importantly, these peak values are comparable or even stronger than those critical $\gamma(\mathbf{q})$ values in MEPC-induced CDW systems, *e.g.*, $1T\text{-TaSe}_2$ [34], $1T\text{-VSe}_2$ [35], and TbTe_3 [36]. When n_h increases, the intensities of these peaks dramatically decrease, and some of them (*e.g.*, A' and C) can even disappear at a high n_h . Therefore, it can be expected that, when $n_h = 0$, the joint contributions of multiple peaks in both $\text{Re}\chi(\mathbf{q})$ and $\gamma(\mathbf{q})$ from multiple q_z planes might play important roles in generating 3D CDW (rather than 2D-like CDWs as commonly observed in cuprates [5]) in NdNiO_2 . When n_h increases, both EI and MEPC are strongly weakened, consequently suppressing the driving forces for CDW formation. Generally, a similar conclusion is found in LaNiO_2 (Supplementary Fig. S4) and, again, the consideration of on-site Hubbard U can further strengthen our conclusion (Supplementary Figs. S6-S7). Oposing to the RNiO_2 , the $\gamma(\mathbf{q})$ of CaCuO_2 are much insensitive to n_h (Supplementary Fig. S8).

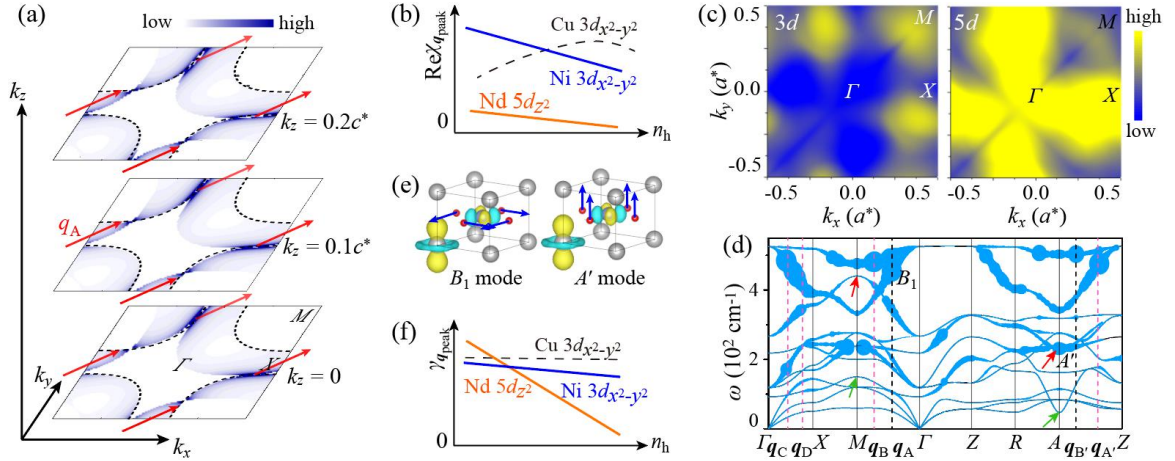


FIG. 3 (a) Evolution of \mathbf{k} -resolved $\text{Re}\chi_{\mathbf{q}}(\mathbf{k})$ at \mathbf{q}_A along different (small) k_z in undoped NdNiO_2 , where $\text{Re}\chi_{\mathbf{q}}(\mathbf{k})$ is projected to $\text{Ni } 3d_{x^2-y^2}$ orbital. Black-dashed lines represent the FS of $\text{Ni } 3d_{x^2-y^2}$ band and red arrows of \mathbf{q}_A connect the electronic states on FS to form a nesting (in view of almost unchanged FS along k_z). (b) Contributions of $\text{Ni } 3d_{x^2-y^2}$ and $\text{Nd } 5d_{z^2}$ to $\text{Re}\chi_{\mathbf{qpeak}}$ as a function of n_h . (c) MEPC matrix $g(\mathbf{k})$ from all the phonon modes at \mathbf{q}_A in $k_z = 0$ plane. (d) Phonon spectrum of undoped NdNiO_2 with the magnitudes of phonon linewidth indicated by the line thickness. (e) Two typical strong orbital-phonon coupling modes at \mathbf{q}_A and $\mathbf{q}_{B'}$, labeled in (d). (f) Contributions of $\text{Ni } 3d_{x^2-y^2}$ and $\text{Nd } 5d_{z^2}$ to $\gamma_{\mathbf{qpeak}}$ as a function of n_h . Contributions of $\text{Cu } 3d_{x^2-y^2}$ to $\text{Re}\chi_{\mathbf{qpeak}}$ and $\gamma_{\mathbf{qpeak}}$

of CaCuO₂ as a function of n_h are also schematically plotted in (b) and (f), respectively, for comparison with the Ni $3d_{x^2-y^2}$ and Nd $5d_{z^2}$ of NdNiO₂.

Mechanism for hole-doping-dependent EI and MEPC. To further investigate the contribution of electronic states to $\text{Re}\chi(\mathbf{q})$ in NdNiO₂, taking peak A as an example (other peaks are similar), the \mathbf{k} -resolved $\text{Re}\chi_{qA}(\mathbf{k})$ for Ni $3d_{x^2-y^2}$ band (a majority contributor) is shown in Fig. 3(a), and the results for Nd $5d_{z^2}$ (a minority contributor) are given in Supplementary Information (Supplementary Figs. S9 and S10). Basically, for a fixed \mathbf{q} , the contributions to $\text{Re}\chi$ can be divided into two parts: (i) states on FS connected by \mathbf{q} [dark-blue spots in Fig. 3(a)]; (ii) occupied and unoccupied states (not on FS) connected by \mathbf{q} [light-blue regions in Fig. 3(a)] (see Supplementary Fig. S9 for details). Importantly, while (i) strongly depends on the shape of FS and determines the peak formation to $\text{Re}\chi$, (ii) is weak and mostly contributes a uniform value to $\text{Re}\chi$. As shown in Fig. 3(a), the unique FS shape of NdNiO₂, induced by the VHS across E_F , makes the states on FS near BZ boundary well connected by \mathbf{q}_A [red arrows in Fig. 3(a)], contributing a large value to $\text{Re}\chi_{qA}$. Importantly, the FS in k_x - k_y plane is almost unchanged with variable k_z between $0 \leq k_z \leq 0.2c^*$ [e.g., parallel lines marked in Fig. 1(b)], and the connection vector \mathbf{q}_A in different k_z planes keeps constant in this FS segment (also see Supplementary Fig. S10 for details), resulting in a strong FSN and contributing a large peak A to $\text{Re}\chi(\mathbf{q})$ [Fig. 2(a)]. As a comparison, the FS of (undoped) CaCuO₂ has a variation with k_z due to the absent VHS across E_F , and the connection vector \mathbf{q} is also changed gradually (Supplementary Fig. S10). Consequently, there is no obvious peak in $\text{Re}\chi(\mathbf{q})$ of undoped CaCuO₂ (Supplementary Figs. S8 and S10).

Under hole doping, the VHS across E_F shifts to a smaller k_z value, which reduces the k_z range for parallel FS segment of $3d_{x^2-y^2}$ band [i.e., the length of parallel lines marked in Fig. 1(b)], thus decreasing the strength of FSN (Supplementary Fig. S11). In addition, hole doping reduces the occupation of Nd $5d_{z^2}$ states at FS, decreasing their sphere-like electron pocket. Fig. 3(b) shows the change of contribution from Ni $3d_{x^2-y^2}$ and Nd $5d_{z^2}$ states to $\text{Re}\chi_{qA}$ (and other peaks) as a function of n_h (also see Supplementary Fig. S10). As n_h increases, the contribution of both Ni $3d_{x^2-y^2}$ and Nd $5d_{z^2}$ decrease, explaining the observation in Fig. 2(a). Meanwhile, as n_h increases, the evolved FS gradually shifts \mathbf{q}_A to smaller values. On the other hand, the opposite trend of $\text{Re}\chi_{qA}$ in CaCuO₂ under hole doping can be well understood as the gradual approach of VHS to E_F and the lack of $5d$ orbital (Supplementary Fig. S11), i.e., a dome region could exist in CaCuO₂ but not in RNiO₂.

In contrast to $\text{Re}\chi_{qA}(\mathbf{k})$, Nd $5d_{z^2}$ plays a larger role in MEPC. As shown in Fig. 3(c), the MEPC matrix $g(\mathbf{k})$ at \mathbf{q}_A obtained from all the phonon modes highlight the major contribution of intraband scattering of Nd $5d_{z^2}$. The magnitude of interband scattering between Ni $3d_{x^2-y^2}$ and Nd $5d_{z^2}$ is similar to the intraband scattering of Ni $3d_{x^2-y^2}$ orbital (Supplementary Figs. S12 and S13). The calculated phonon spectrum of undoped NdNiO₂ is shown in Fig. 3(d). Comparing the phonon dispersion between $k_z = 0$ and $k_z = 0.5c^*$ planes, it is clearly identified that there are two strongly soft optical modes around A, as indicated by the arrows. The projected $\gamma(\mathbf{q})$ shows that the main contribution comes from optical modes. Importantly, one soft mode partially contributes to the large γ_{qB} . The phonon spectrum of LaNiO₂ along with the projected $\gamma(\mathbf{q})$ are similar to that of

NdNiO₂ (Supplementary Fig. S14). Importantly, the appearance of soft optical modes is also observed in CDW-phase LaNiO₂ in experiments [11].

Figure 3(e) shows the two typical strong orbital-phonon coupling (OPC) modes at q_A and q_B , as marked in Fig. 3(d). Similar to that in cuprates [37], due to the large mass differences between Nd/Ni and O atoms, the atomic vibrations are much stronger for O atoms. While the orbital components in both modes come from the Nd $5d_{z^2}$ and Ni $3d_{x^2-y^2}$, the phonon modes can be either in-plane B_1 mode or out-of-plane A' mode. The B_1 mode contributes large EPC, and the A' mode relates to the soft phonon. When n_h increases, the phonon spectrum of NdNiO₂ only has small changes (Supplementary Fig. S14), but the occupation of Nd $5d_{z^2}$ around E_F dramatically decreases. Consequently, as shown in Fig. 3(f), the γ_{q_A} decreases rapidly, explaining the observation in Figs. 2(c) and (d). On the other hand, the lack of Ca $5d_{z^2}$ around E_F can explain the much insensitivity of γ_q under different n_h in CaCuO₂ (Supplementary Fig. S8).

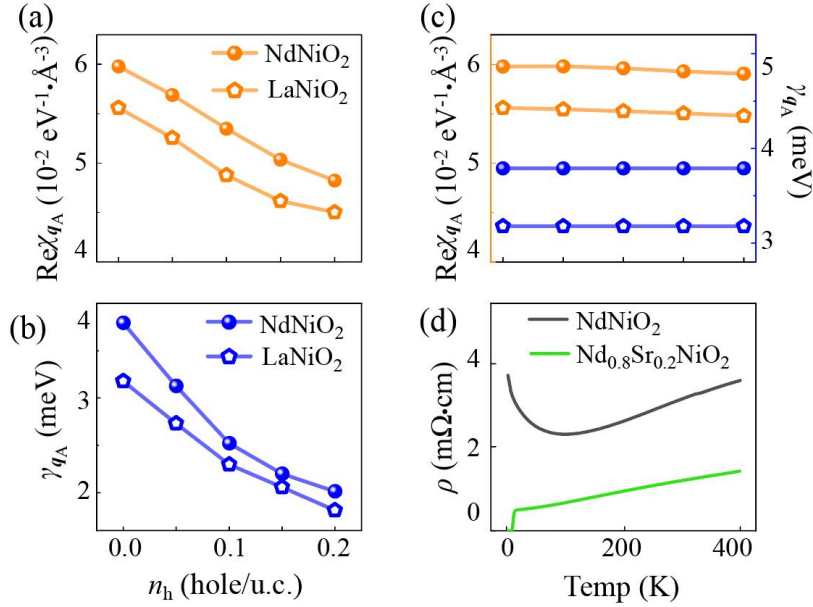


FIG. 4 Comparison of calculated (a) $\text{Re}\chi_{q_A}$ and (b) γ_{q_A} for NdNiO₂ and LaNiO₂ as a function of n_h . (c) Calculated $\text{Re}\chi_{q_A}$ and γ_{q_A} as a function of temperature. (d) Experimentally measured electrical resistivity of NdNiO₂ (with CDW) and Nd_{0.8}Sr_{0.2}NiO₂ (without CDW) as a function of temperature.

Comparison between NdNiO₂ and LaNiO₂. It is interesting to compare the calculated $\text{Re}\chi(q)$ and $\gamma(q)$ between NdNiO₂ and LaNiO₂. Overall, the spectra of $\text{Re}\chi(q)$ or $\gamma(q)$ are similar for both systems, except for the specific values. As shown in Figs. 4(a) and 4(b), the values of $\text{Re}\chi_{q_A}$ and γ_{q_A} in LaNiO₂ are smaller than that of NdNiO₂, mostly because the occupation of La $5d_{z^2}$ is smaller than that of Nd $5d_{z^2}$ [Fig. 1(b)]. Under hole doping, obeying the mechanism discussed above, the values of $\text{Re}\chi_{q_A}$ and γ_{q_A} will gradually decrease in both systems, accompanied by the decreases of q_A . Generally, the trend of other peaks in $\text{Re}\chi_q$ and γ_q and their n_h -dependent behaviors (Supplementary Fig. S15) are similar to that of $\text{Re}\chi_{q_A}$.

Unexpectedly, as shown in Fig. 4(c), the values of $\text{Re}\chi_{qA}$ and γ_{qA} are estimated to be insensitive to the electron temperature even up to 400 K for the undoped $R\text{NiO}_2$ (similar for other q values, Supplementary Fig. S16), indicating the strong EI and MEPC may maintain above room temperature. Therefore, if the CDWs observed in $R\text{NiO}_2$ partially originate from the EI and MEPC, it may also survive at high temperature. In experiments, the undoped NdNiO_2 grown on SrTiO_3 substrate (without STO capping layers) may exhibit a CDW phase [12]. To confirm our theory, we perform the transport measurements using a similar CDW-phase NdNiO_2 sample adopted in Ref. 12 (see Methods). As shown in Fig. 4(d), no signal of a sharp phase transition is observed up to 400 K in the electrical resistivity, indicating that the CDW phase in NdNiO_2 might survive at such a high temperature. For our $\text{Nd}_{0.8}\text{Sr}_{0.2}\text{NiO}_2$ sample with a superconducting temperature of ~ 10 K, the CDW phase is not observed to coexist with the superconductivity using RIXS measurement [12], possibly due to their competitive relationship and/or largely reduced EI and MEPC in heavy-hole-doped $R\text{NiO}_2$.

Discussion and Outlook. It is important to compare our theory with the existing experimental observations. First, it is observed in experiments that the $R 5d_{z^2}$ and $\text{Ni } 3d_{x^2-y^2}$ orbitals are resonant during the formation of CDWs in $R\text{NiO}_2$ [11,12], consistent with our theoretical calculations. More importantly, beyond the experimental observations, our theory further reveals that the $\text{Ni } 3d_{x^2-y^2}$ [Fig. 3(a)] and $R 5d_{z^2}$ [Fig. 3(c)] play the major role in forming strong EI and MEPC in undoped $R\text{NiO}_2$, respectively, which may in turn result in a very high temperature CDW phase (at least) up to 400 K, as confirmed by our preliminary experimental measurements. In comparison, the CDWs observed in cuprates usually cannot exist above ~ 250 K [4,5].

Second, it is observed in experiments that hole doping gradually destabilizes or even suppresses the CDW phase in $R\text{NiO}_2$ [11,12], which is strongly different from (even opposite to) that in cuprates [5,14]. It may also be explained by our theory. Especially, our theory demonstrates that as n_h increases, the shift of VHS and the rapidly decrease of $R 5d_{z^2}$ orbital at FS largely weaken EI [Fig. 3(b)] and MEPC [Fig. 3(f)] in $R\text{NiO}_2$, respectively, suppressing the driving forces for CDW formation in $R\text{NiO}_2$. We note that the part role of strong correlation effect in CDW formation may not be excluded, even there is no direct evidence that it is a significant change of correlation by hole doping [20,21] that suppress the CDWs. Again, the recent calculations from both hybrid functional and dynamical mean-field theory [30,31] present almost the same low-energy electronic structure and FS as ours.

Finally, it is still a challenge to directly identify the q_{CDW} based on our calculations, as it likely be a combination of several similar low-energy CDW excitations at multiple peaks in multiple q_z planes of $\text{Re}\chi_q$ and γ_q . These multiple peaks also indicate that multiple q_{CDW} might appear under different conditions, calling for future experimental verification. However, our theory predicts that the q_{CDW} in LaNdO_2 and NdNiO_2 could be very similar due to their nearly identical peaks in $\text{Re}\chi(q)$ and $\gamma(q)$, consistent with the experimental observations [11,12]. In practice, the exact q_{CDW} could also highly depend on the local environments, defects (*e.g.*, possible H impurity [13,38]), and structural disorders [11,39], which are not included in the present study.

Acknowledgement. We thank Dr. J. G. Guo at IOP for the help on the measurements of electrical resistivity of NdNiO_2 and $\text{Nd}_{0.8}\text{Sr}_{0.2}\text{NiO}_2$ at different temperatures and Dr. Z. Liu at Tsinghua University for the valuable comments on our results. We acknowledge the support from the NSFC (12004030, 12088101) and the NSAF (U1930402). The calculations were performed at Tianhe2-JK at CSRC.

References

- [1] J. G. Bednorz and K. A. Müller, Possible high T_c superconductivity in the Ba–La–Cu–O system. *Z. Phys. B-Condens. Matter* **64**(2), 189 (1986).
- [2] M. Azuma, Z. Hiroi, M. Takano, Y. Bando, and Y. Taketa, Superconductivity at 110K in the infinite-layer compound $(\text{Sr}_{1-x}\text{Ca}_x)_{1-y}\text{CuO}_2$. *Nature (London)* **356**, 775 (1992).
- [3] N. Damascelli, Z. Hussain, and Z.-X. Shen, Angle-resolved photoemission studies of the cuprate superconductors. *Rev. Mod. Phys.* **75**(2), 473 (2003).
- [4] E. Fradkin, S. A. Kivelson, and J. M. Tranquada, Theory of intertwined orders in high temperature superconductors. *Rev. Mod. Phys.* **87**(2), 457 (2015).
- [5] R. Comin, and A. Damascelli, Resonant X-ray scattering studies of charge order in cuprates. *Annu. Rev. Condens. Matter Phys.* **7**(1), 369 (2016).
- [6] V. I. Anisimov, D. Bukhvalov, and T. M. Rice, Electronic structure of possible nickelate analogs to the cuprates. *Phys. Rev. B* **59**, 7901 (1999).
- [7] M. A. Hayward, M. A. Green, M. J. Rosseinsky, and J. Sloan, Sodium hydride as a powerful reducing agent for topotactic oxide deintercalation: Synthesis and characterization of the Nickel(I) oxide LaNiO_2 . *J. Am. Chem. Soc.* **121**, 8843(1999).
- [8] D. Li, K. Lee, B. Y. Wang, M. Osada, S. Crossley, H. R. Lee, Y. Cui, Y. Hikita, and H. Y. Hwang, Superconductivity in an infinite-layer nickelate. *Nature (London)* **572**, 624 (2019).
- [9] M. Osada, B. Y. Wang, Be. H. Goodge, S. P. Harvey, K. o Lee, D. Li, L. F. Kourkoutis, and H. Y. Hwang, Nickelate superconductivity without rare-earth magnetism: $(\text{La},\text{Sr})\text{NiO}_2$. *Adv. Mater.* **33**, 45, (2021).
- [10] K. McElroy, D.-H. Lee, J. E. Hoffman, K. M. Lang, J. Lee, E. W. Hudson, H. Eisaki, S. Uchida, and J. C. Davis, Coincidence of checkerboard charge order and antinodal state decoherence in strongly underdoped superconducting $\text{Bi}_2\text{Sr}_2\text{CaCu}_2\text{O}_8$. *Phys. Rev. Lett.* **94**, 197005 (2005).
- [11] M. Rossi, M. Osada, J. Choi, S. Agrestini, D. Jost, Y. Lee, H. Lu, B. Y. Wang, K. Lee, A. Nag, Y.-D. Chuang, C.-T. K., S.-J. Lee, B. Moritz, T. P. Devereaux, Z.-X. Shen, J.-S. Lee, K.-J. Zhou, H. Y. Hwang and W.-S. Lee, A broken translational symmetry state in an infinite-layer nickelate. *arXiv: 2112.02484*.
- [12] C. C. Tam, J. Choi, X. Ding, S. Agrestini, A. Nag, B. Huang, H. Luo, M. G.-Fernández, L. Qiao, and K.-J. Zhou, Charge density waves in infinite-layer NdNiO_2 nickelates. *arXiv: 2112.04440*.
- [13] G. Krieger, L. Martinelli, S. Zeng, L. E. Chow, K. Kummer, R. Arpaia, M. Moretti Sala, N.B. Brookes, A. Ariando, N. Viart, M. Salluzzo, G. Ghiringhelli, and D. Preziosi, Charge and spin order dichotomy in NdNiO_2 driven by SrTiO_3 capping layer. *arXiv: 2112.03341*.
- [14] S. Badoux, S. A. A. Afshar, B. Michon, A. Ouellet, S. Fortier, D. LeBoeuf, T. P. Croft, C. Lester, S. M. Hayden, H. Takagi, K. Yamada, D. Graf, N. Doiron-Leyraud, and L. Taillefer, Critical doping for the onset of Fermi-surface reconstruction by charge-density-wave order in the cuprate superconductor $\text{La}_{2-x}\text{Sr}_x\text{CuO}_4$. *Phy. Rev. X* **6**, 021004 (2016).

- [15] R. Raimondi, C. Castellani, and M. Grilli, Charge collective modes and dynamic pairing in the three-band Hubbard model. II. Strong-coupling limit. *Phys. Rev. B* **47**(6), 3331 (1993).
- [16] A. Lanzara, P. V. Bogdanov, X. J. Zhou, S. A. Kellar, D. L. Feng, E. D. Lu, T. Yoshida, H. Eisaki, A. Fujimori, K. Kishio, J.-I. Shimoyama, T. Noda, S. Uchida, Z. Hussain, and Z.-X. Shen, Evidence for ubiquitous strong electron-phonon coupling in high-temperature superconductors. *Nature (London)* **412**, 510 (2001).
- [17] C. C. Tam, M. Zhu, J. Ayres, K. Kummer, F. Yakhov-Harris, J. R. Cooper, A. Carrington, and S. M. Hayden, Charge density waves and Fermi surface reconstruction in the clean overdoped cuprate superconductor $\text{Tl}_2\text{Ba}_2\text{CuO}_{6+\delta}$. *Nat. Commun.* **13**, 570 (2022).
- [18] T. M. Rice, and G. K. Scott, New mechanism for a charge-density-wave instability. *Phys. Rev. Lett.* **35**, 2 (1975).
- [19] X. Zhua, Y. Cao, J. Zhang, E. W. Plummerb, and J. Guo, Classification of charge density waves based on their nature. *Proc. Natl. Acad. Sci. U.S.A.* **112**(8), 2367 (2015).
- [20] M. Rossi, H. Lu, A. Nag, D. Li, M. Osada, K. Lee, B. Y. Wang, S. Agrestini, M. Garcia-Fernandez, J. J. Kas, Y.-D. Chuang, Z. X. Shen, H. Y. Hwang, B. Moritz, K.-J. Zhou, T. P. Devereaux, and W. S. Lee, Orbital and spin character of doped carriers in infinite-layer nickelates. *Phys. Rev. B* **104**, L220505 (2021).
- [21] K.-W. Lee and W. E. Pickett, Infinite-layer LaNiO_2 : Ni^{1+} is not Cu^{2+} . *Phys. Rev. B* **70**, 165109 (2004).
- [22] A. H. Castro Neto, Charge density wave, superconductivity, and anomalous metallic behavior in 2D transition metal dichalcogenides. *Phys. Rev. Lett.* **86**, 19 (2001).
- [23] J. G. Si, W. J. Lu, H. Y. Wu, H. Y. Lv, X. Liang, Q. J. Li, and Y. P. Sun, Origin of the multiple charge density wave order in 1T-VSe_2 . *Phys. Rev. B* **101**, 235405 (2020).
- [24] A. S. Botana¹ and M. R. Norman, Similarities and differences between LaNiO_2 and CaCuO_2 and implications for Superconductivity. *Phys. Rev. X* **10**, 011024 (2020).
- [25] M. Hepting, D. Li, C. J. Jia, H. Lu, E. Paris, Y. Tseng, X. Feng, M. Osada, E. Been, Y. Hikita, Y.-D. Chuang, Z. Hussain, K. J. Zhou, A. Nag, M. Garcia-Fernandez, M. Rossi, H. Y. Huang, D. J. Huang, Z. X. Shen, T. Schmitt, H. Y. Hwang, B. Moritz, J. Zaanen, T. P. Devereaux, and W. S. Lee, Electronic structure of the parent compound of superconducting infinite-layer nickelates. *Nat. Mater.* **19**, 381 (2020).
- [26] G.-M. Zhang, Y. Yang, and F.-C. Zhang, Self-doped Mott insulator for parent compounds of nickelate superconductors. *Phys. Rev. B* **101**, 020501(R) (2020).
- [27] P. A. Lee, N. Nagaosa, and X-G. Wen, Doping a Mott insulator: Physics of high-temperature superconductivity. *Rev. Mod. Phys.* **78**(1), 17 (2006).
- [28] J. Karp, A. S. Botana, M. R. Norman, H. Park, M. Zing, and A. Millis, Many-body electronic structure of NdNiO_2 and CaCuO_2 . *Phys. Rev. X* **10**, 021061 (2020).
- [29] H. Sakakibara, H. Usui, K. Suzuki, T. Kotani, H. Aoki, and K. Kuroki, Model construction and a possibility of cupratelike pairing in a new d^9 nickelate superconductor $(\text{Nd,Sr})\text{NiO}_2$. *Phys. Rev. Lett.* **125**, 077003 (2020).
- [30] H. Zhang, L. Jin, S. Wang, B. Xi, X. Shi, F. Ye, and J.-W. Mei, Effective Hamiltonian for nickelate oxides $\text{Nd}_{1-x}\text{Sr}_x\text{NiO}_2$. *Phys. Rev. Research* **2**, 013214 (2020).
- [31] Z. Liu, C. Xu, C. Cao, W. Zhu, Z. F. Wang, and J. Yang, Doping dependence of electronic structure of infinite-layer NdNiO_2 . *Phys. Rev. B* **103**, 045103 (2021).

- [32] H. Lu, M. Rossi, A. Nag, M. Osada, D. F. Li, K. Lee, B. Y. Wang, M. Garcia-Fernandez, S. Agrestini, Z. X. Shen, E. M. Been, B. Moritz, T. P. Devereaux, J. Zaanen, H. Y. Hwang, Ke-Jin Zhou, and W. S. Lee, Magnetic excitations in infinite-layer nickelates. *Science* **373**, 213 (2021).
- [33] A. Ricci, N. Poccia, G. Campi, S. Mishra, L. Müller, B. Joseph, B. Shi, A. Zozulya, M. Buchholz, C. Trabant, J. C. T. Lee, J. Viehhaus, J. B. Goedkoop, A. A. Nugroho, M. Braden, S. Roy, M. Sprung, and C. Schüßler-Langeheine, Measurement of spin dynamics in a layered nickelate using X-ray photon correlation spectroscopy: Evidence for intrinsic destabilization of incommensurate stripes at low temperatures. *Phys. Rev. Lett.* **127**, 057001 (2021).
- [34] Y. Liu, D. F. Shao, L. J. Li, W. J. Lu, X. D. Zhu, P. Tong, R. C. Xiao, L. S. Ling, C. Y. Xi, L. Pi, H. F. Tian, H. X. Yang, J. Q. Li, W. H. Song, X. B. Zhu, and Y. P. Sun, Nature of charge density waves and superconductivity in $1T\text{-TaSe}_{2-x}\text{Te}_x$. *Phys. Rev. B* **94**, 045131 (2016).
- [35] Z. Wang, J. Zhou, K. P. Loh, and Y. P. Feng, Controllable phase transitions between multiple charge density waves in monolayer $1T\text{-VSe}_2$ via charge doping. *Appl. Phys. Lett.* **119**, 163101 (2021).
- [36] M. Maschek, S. Rosenkranz, R. Heid, A. H. Said, P. Giraldo-Gallo, I. R. Fisher, and F. Weber, Wave-vector-dependent electron-phonon coupling and the charge-density-wave transition in TbTe_3 . *Phys. Rev. B* **91**, 235146 (2015).
- [37] D. Reznik, L. Pintschovius, M. Ito, S. Iikubo, M. Sato, H. Goka, M. Fujita, K. Yamada, G. D. Gu, and J. M. Tranquada, Electron-phonon coupling reflecting dynamic charge inhomogeneity in copper oxide superconductors. *Nature* **440**, 1170 (2006).
- [38] L. Si, W. Xiao, J. Kaufmann, J. M. Tomczak, Y. Lu, Z. Zhong, and K. Held, Topotactic hydrogen in nickelate superconductors and akin infinite-layer oxides ABO_2 . *Phys. Rev. Lett.* **124**, 166402 (2020).
- [39] B. H. Goodge, B. Geisler, K. Lee, M. Osada, B. Y. Wang, D. Li, H. Y. Hwang, R. Pentcheva, and L. F. Kourkoutis, Reconstructing the polar interface of infinite-layer nickelate thin films. arXiv: 2201.03613.

Methods

1. Computational methods

All the electronic structures and crystal structure optimizations are performed using the first-principles calculations as implemented in the Quantum ESPRESSO (QE) [40], and the scalar relativistic ultrasoft pseudopotentials are used [41]. The kinetic energy cutoff for plane waves is set to 80 Ry. Some calculations are also tested using the Vienna ab initio simulation package (VASP) [42] within the projector augmented wave method [43] and Perdew-Burke-Ernzerhof [44] exchange correlation functional, which give the same results as QE. The lattice constants in xy plane are fixed at $a = b = 3.905 \text{ \AA}$ to match the SrTiO₃ substrate, while lattice in z direction is fully relaxed, which gives $c = 3.34 \text{ \AA}$ and 3.45 \AA for NdNiO₂ and LaNiO₂, respectively. The van der Waals correction is adopted [45]. The electron-phonon coupling calculations are performed by Wannier interpolation [46,47], as implemented in EPW code [48], which allows us to achieve sufficiently accurate k -point sampling in the BZ. The calculations of the phonon linewidth are performed on dense grids of $(100 \times 100 \times 100)$ k -points and $(100 \times 100 \times 1)$ q -points. The on-site Hubbard U [49,50] is also considered, which is added on the $3d$ orbitals of Ni. The temperature effect is considered as implemented in the Fermi-Dirac distribution.

The real $\text{Re}\chi(\mathbf{q})$ and imaginary $\text{Im}\chi(\mathbf{q})$ part of electron susceptibility [51] are calculated by

$$\text{Re}\chi(\mathbf{q}) = \sum_{\mathbf{k}} \frac{f(\varepsilon_{\mathbf{k}}) - f(\varepsilon_{\mathbf{k}+\mathbf{q}})}{\varepsilon_{\mathbf{k}} - \varepsilon_{\mathbf{k}+\mathbf{q}}} \quad (1)$$

$$\text{Im}\chi(\mathbf{q}) = \sum_{\mathbf{k}} \delta(\varepsilon_{\mathbf{k}} - \varepsilon_F) \delta(\varepsilon_{\mathbf{k}+\mathbf{q}} - \varepsilon_F),$$

where $f(\varepsilon_{\mathbf{k}})$ is the function of Fermi-Dirac distribution. The real part reflects the stability of the electronic system, and the imaginary part reflects the Fermi surface topology of a system. The phonon linewidth $\gamma(\mathbf{q})$ which directly reflects the electron-phonon coupling strength is defined as

$$\gamma(\mathbf{q}, \nu) = 2\pi\omega_{\mathbf{q}\nu} \sum_{mn} \int \frac{d\mathbf{k}}{\Omega_{BZ}} |g_{mn,\mathbf{q}\nu}(\mathbf{k})|^2 \times \delta(\varepsilon_{m,\mathbf{k}} - \varepsilon_F) \delta(\varepsilon_{n,\mathbf{k}+\mathbf{q}} - \varepsilon_F), \quad (2)$$

where m, n are the band indexes, and ν represents the phonon mode. The coupling matrix is

$$g_{mn,\mathbf{q}\nu}(\mathbf{k}) = \frac{1}{\sqrt{2\omega_{\mathbf{q}\nu}}} \langle \varphi_{m,\mathbf{k}} | \partial_{\mathbf{q}\nu} V | \varphi_{n,\mathbf{k}+\mathbf{q}} \rangle. \quad (3)$$

The $\varphi_{m,\mathbf{k}}$ is the electronic wave function, with eigenvalue $\varepsilon_{m,\mathbf{k}}$.

2. Experimental methods

The NdNiO₂ films with infinite-layer structure are prepared by topochemical reduction of perovskite NdNiO₃ without capping layer. NdNiO₃ films (thickness about 10 nm) are deposited on TiO₂-terminated STO (001) substrates by 248-nm KrF laser. During the deposition, the substrate temperature is controlled at 620 °C with the oxygen pressure of 200 mTorr. A laser fluence of 1.2 J/cm² is used to ablate the target and the size of laser spot is about 3 mm². After deposition, the samples are cooled down in the same oxygen pressure at the rate of 10 °C/min. In order to acquire the infinite-layer nickelate phase, the as-grown samples are sealed in the quartz tube together with

0.1g CaH₂. The pressure of the tube is about 0.3 mTorr. Then, the tube is heat up to 290 °C in tube furnace and hold for 2 hours and cooled down naturally with the ramp rate of 10 °C/min. The superconducting Nd_{0.8}Sr_{0.2}NiO₂ films are prepared in the same way as the parent NdNiO₂. The crystal structures of films are characterized using a Bruker D8 Discover diffractometer. The temperature-dependent resistivity is measured using four-probe method in a physical properties measurement system (PPMS, Quantum Design Inc.).

References

- [40] G. Paolo, B. Stefano, B. Nicola, C. Matteo, C. Roberto, C. Carlo, C. Davide, L. C. Guido, C. Matteo, D. Ismaila, C. AndreaDal, G. Stefano de, F. Stefano, F. Guido, G. Ralph, G. Uwe, G. Christos, K. Anton, L. Michele, M.-S. Layla, M. Nicola, M. Francesco, M. Riccardo, P. Stefano, P. Alfredo, P. Lorenzo, S. Carlo, S. Sandro, S. Gabriele, P. S. Ari, S. Alexander, U. Paolo, and M. W. Renata, QUANTUM ESPRESSO: a modular and open-source software project for quantum simulations of materials. *J. Phys.: Condens. Matter* **21**, 395502 (2009).
- [41] D. Vanderbilt, Soft self-consistent pseudopotentials in a generalized eigenvalue formalism. *Phys. Rev. B* **41**, 7892 (1990).
- [42] G. Kresse, G. and J. Furthmuller, Efficient iterative schemes for ab initio total-energy calculations using a plane-wave basis set. *Phys. Rev. B* **54**, 11169 (1996).
- [43] P. E. Blöchl, Projector augmented-wave method. *Phys. Rev. B* **50**, 17953 (1994).
- [44] J. P. Perdew, K. Burke, and M. Ernzerhof, Generalized Gradient Approximation Made Simple. *Phys. Rev. Lett.* **77**, 3865 (1996).
- [45] S. Grimme, J. Antony, S. Ehrlich, and S. Krieg, A consistent and accurate *ab initio* parametrization of density functional dispersion correction (DFT-D) for the 94 elements H-Pu. *J. Chem. Phys.* **132**, 154104 (2010).
- [46] S. Baroni, S. De Gironcoli, A. Dal Corso, and P. Giannozzi, Phonons and related crystal properties from density-functional perturbation theory. *Rev. Mod. Phys.* **73**, 515 (2001).
- [47] F. Giustino, M. L. Cohen, and S. G. Louie, Electron-phonon interaction using Wannier functions. *Phys. Rev. B* **76**, 165108 (2007).
- [48] S. Poncé, E. R. Margine, C. Verdi, and F. Giustino, EPW: Electronphonon coupling, transport and superconducting properties using maximally localized Wannier functions. *Comput. Phys. Commun.* **209**, 116 (2016).
- [49] V. Anisimov, I., J. Zaanen, and O. K. Anderson, Band theory and Mott insulators: Hubbard U instead of Stoner I. *Phys. Rev. B* **44**, 943 (1991).
- [50] V. I. Anisimov, A. I. Poteryaev, M. A. Korotin, A. O. Anokhin, and G. Kotliar, First-principles calculations of the electronic structure and spectra of strongly correlated systems: dynamical mean-field theory. *J. Phys.: Condens. Matter* **9**, 7359 (1997).
- [51] M. D. Johannes, and I. I. Mazin, Fermi surface nesting and the origin of charge density waves in metals. *Phys. Rev. B* **77**, 165135 (2008).